


RESEARCH ARTICLE

# Performance evaluation and dimensional optimization design of planar 6R redundant actuation parallel mechanism

Ming Han , Jiajin Che, Jinyue Liu and Dong Yang

School of Mechanical Engineering, Hebei University of Technology Tianjin, China

**Corresponding authors:** Jinyue Liu; Email: [ljj@hebut.edu.cn](mailto:ljj@hebut.edu.cn), Dong Yang; Email: [yd@hebut.edu.cn](mailto:yd@hebut.edu.cn)

**Received:** 6 December 2023; **Revised:** 3 February 2024; **Accepted:** 2 March 2024; **First published online:** 27 March 2024

**Keywords:** motion/force transmission performance; redundant drive; good transmission workspace; performance map; scale optimization

## Abstract

Aiming at the problems of small good workspace, many singular configurations, and limited carrying capacity of non-redundant parallel mechanisms, a full-redundant drive parallel mechanism is designed and developed, and its performance evaluation, good workspace identification, and scale optimization design are studied. First, the kinematics analysis of the planar 6R parallel mechanism is completed. Then, the motion/force transmission performance evaluation index of the mechanism is established, and the singularity analysis of the mechanism is completed. Based on this, the fully redundant driving mode of the mechanism is determined, and the good transmission workspace of the mechanism in this mode is identified. Then, the mapping relationship between the performance and scale of the mechanism is established by using the space model theory, and the scale optimization of the mechanism is completed. Finally, the robot prototype is made according to the optimal scale, and the performance verification is carried out based on the research of dynamics and control strategy. The results show that the fully redundant actuation parallel mechanism obtained by design optimization has high precision and large bearing capacity. The position repeatability and position accuracy are 0.053 mm and 0.635 mm, respectively, and the load weight ratio can reach 15.83%. The research results of this paper complement and improve the performance evaluation and scale optimization system of redundantly actuated parallel mechanisms.

## 1. Introduction

Currently, research on performance evaluation and scale optimization methods for parallel mechanisms mainly focuses on non-redundant parallel mechanisms. However, non-redundant parallel mechanisms suffer from issues such as limited workspace, high singularity occurrence, and restricted load-bearing capacity, which fail to meet practical needs [1–4]. Therefore, there is an urgent need to design and develop a fully redundant drive parallel mechanism and investigate issues related to performance evaluation metrics, identification of good workspace, and scale-optimized design [5–7].

Performance analysis is a crucial aspect of mechanism design and a key step in achieving scale optimization [8–9]. Building on kinematic analysis, establishing performance evaluation metrics is a prerequisite for optimizing the design of parallel mechanisms [10–11]. These mechanisms primarily employ the mathematical characteristics of Jacobian matrices and motion/force transmission properties to evaluate their kinematic performance. For non-redundant parallel mechanisms, Nabavi *et al.* [12] employed the characteristic length method to establish dimensionless Jacobian matrices for a 6-degrees of freedom (DOF) PUS parallel mechanism and analyzed the performance metrics of manipulability and workspace. Antonov *et al.* [13], using both the characteristic length and linear velocity mapping

methods, constructed dimensionless Jacobian matrices for a 6-DOF parallel mechanism, investigating workspace and singularity. However, due to the inconsistent dimensionalities of elements in the Jacobian matrix of parallel mechanisms with rotational coupling, performance evaluation metrics fail to clearly represent the mapping between kinematic performance in joint space and operational space [14]. Motion and force transmission/constraint properties not only reflect the mapping of motion and force between joint space and operational space but also serve as the basis for identifying good workspace and singular spaces [15]. For instance, Wang *et al.* [16] defined performance metrics such as mechanism input, output, and local motion/force transmission characteristics for a planar 5R parallel robot. Using performance maps, they determined the mechanism's geometric parameters. For redundant drive parallel mechanisms, Zhang *et al.* [17] proposed a motion/force transmission performance evaluation method based on screw theory for a novel 1T2R redundant overconstrained parallel mechanism with 3 DOF.

Scale optimization enhances the motion performance of parallel mechanisms, and reasonable geometric parameters are the foundation for achieving optimal performance [18]. Scale optimization methods mainly include the objective function approach and the performance map approach [19]. For example, Fang *et al.* [20] optimized parameters for a 5PUS-PRPU parallel mechanism using the objective function method and through comparative analysis of the workspace before and after optimization validated the correctness of the approach. Yang *et al.* [21] introduced a novel 3-DOF translational parallel robot, proposing a composite evaluation function considering factors such as workspace area, transmission efficiency, and reaction forces to achieve scale optimization for the translational manipulator. While the performance map approach is challenging to apply to mechanisms with more than four design parameters, it visually depicts the relationship between design parameters and performance metrics in a graphical manner [22]. Liu *et al.* [23], for example, established dimensionless design spaces for various parallel mechanisms and systematically studied multiple performance metrics, generating performance maps to achieve scale optimization. Zhu *et al.* [24] studied the mapping relationship between various performance metrics and dimensions for the redundant drive parallel mechanism (R5LD), generating and analyzing corresponding performance maps to identify optimal size regions and complete mechanism optimization. They further conducted an in-depth study of load-bearing capacity and workspace.

The rest of this article is distributed as follows: in the second section, the kinematics analysis of the planar 6R parallel mechanism is completed. In the third section, the local and global performance evaluation indexes of motion/force transmission performance are established, and the singularity of the mechanism is analyzed, and the identification rules of the good transmission workspace (GTW) of the mechanism are formulated. In the fourth section, a scale optimization method based on performance map and high-quality scale domain is proposed to realize the optimization design of mechanism scale parameters. In the fifth section, the prototype of the redundantly actuated parallel robot is completed, and the performance verification is carried out on the basis of the research of mechanism dynamics and control strategy. The last section gives the conclusion of this paper.

## 2. Kinematics analysis

The structure of the planar 6R mechanism is shown in Fig. 1. First, the position of the planar 6R mechanism is analyzed. The joints  $A_1, B_1, A_2$  are the active joint, the joints  $B_2, C_1, C_2$  are the active joint, and the rod  $C_1C_2$  is the moving platform of the mechanism. Its center point  $P$  is the moving platform reference point. The lever  $A_1A_2$  is the frame. A fixed reference coordinate system  $o-xy$  is established. The coordinate origin is located at the center of  $A_1A_2$ .  $x$ -Axis is along  $A_1A_2$  direction and  $y$  axis is perpendicular to  $A_1A_2$ . Suppose  $A_1B_1=A_2B_2=r_1$ ,  $C_1C_2=2r_3$ ,  $B_1C_1=B_2C_2=r_2$ , and  $A_1A_2=2r_4$ .

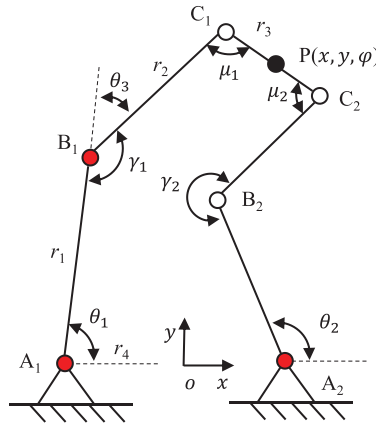


Figure 1. Schematic diagram of planar 6R parallel mechanism.

The center coordinate of rod  $C_1C_2$  is  $P = (x, y, \varphi)$ , where  $\varphi$  is the rotation angle of the moving platform, and the coordinates of each position point are as follows:

$$\begin{cases} \mathbf{a}_1 = (-r_4, 0)^T \\ \mathbf{b}_1 = (r_1 \cos \theta_1 - r_4, r_1 \sin \theta_1)^T \\ \mathbf{c}_1 = (x - r_3 \cos \varphi, y - r_3 \sin \varphi)^T \\ \mathbf{a}_2 = (r_4, 0)^T \\ \mathbf{b}_2 = (r_1 \cos \theta_2 + r_4, r_1 \sin \theta_2)^T \\ \mathbf{c}_2 = (x + r_3 \cos \varphi, y + r_3 \sin \varphi)^T \end{cases} \quad (1)$$

In Eq. (1),  $\theta_1$  and  $\theta_2$  represent the angles between the rod  $A_1A_2$  and the rod  $A_1B_1$  and the rod  $A_1B_2$ , respectively.

From the rod length relationship:

$$|b_1c_1|^2 = |b_2c_2|^2 = r_2^2 \quad (2)$$

Namely:

$$\begin{aligned} & -2r_1(y - r_3 \sin \varphi) \sin \theta_1 - 2r_1(x - r_3 \cos \varphi + r_4) \cos \theta_1 \\ & + (x - r_3 \cos \varphi + r_4)^2 + (y - r_3 \sin \varphi)^2 + r_1^2 - r_2^2 = 0 \end{aligned} \quad (3)$$

Let

$$\begin{cases} A_1 = (x - r_3 \cos \varphi + r_4)^2 + (y - r_3 \sin \varphi)^2 + r_1^2 - r_2^2 \\ B_1 = -2r_1(x - r_3 \cos \varphi + r_4) \\ C_1 = -2r_1(y - r_3 \sin \varphi) \end{cases} \quad (4)$$

Eq. (3) can be written as:

$$C_1 \sin \theta_1 + B_1 \cos \theta_1 + A_1 = 0 \quad (5)$$

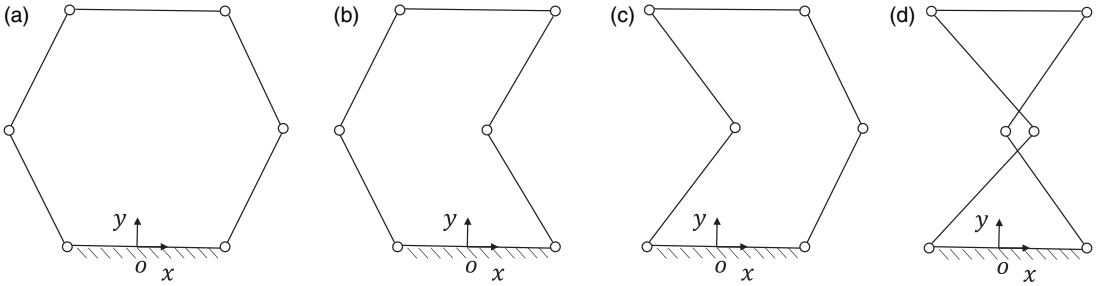


**Figure 2.** Four groups of reverse assembly configurations: (a) ‘+–’ assembly configuration; (b) ‘++’ assembly configuration; (c) ‘--’ assembly configuration; (d) ‘-+’ assembly configuration.

Combined with the double angle equation, let

$$\begin{cases} \sin \theta_1 = \frac{2 \tan\left(\frac{\theta_1}{2}\right)}{1 + \tan^2\left(\frac{\theta_1}{2}\right)} \\ \cos \theta_1 = \frac{1 - \tan^2\left(\frac{\theta_1}{2}\right)}{1 + \tan^2\left(\frac{\theta_1}{2}\right)} \end{cases} \quad (6)$$

By solving Eqs. (5) and (6) simultaneously, we can get

$$\begin{cases} \theta_1 = 2 \arctan \frac{-C_1 \pm \sqrt{C_1^2 + B_1^2 - A_1^2}}{A_1 - B_1} & A_1 \neq B_1 \\ \theta_1 = 2 \arctan \frac{-(A_1 + B_1)}{2C_1} & A_1 = B_1 \end{cases} \quad (7)$$

Similarly available:

$$\theta_3 = \arctan \frac{y - r_3 \sin \varphi - r_1 \sin \theta_1}{x - r_3 \cos \varphi + r_4 - r_1 \cos \theta_1} \quad (8)$$

In addition, it can be solved by cosine theorem:

$$\begin{aligned} \gamma_1 &= \arccos\left(\frac{r_1^2 + r_2^2 - |a_1 c_1|^2}{2r_1 r_2}\right) \\ &= \arccos\left(\frac{r_1^2 + r_2^2 - (x - r_3 \cos \varphi + r_4)^2 - (y - r_3 \sin \varphi)^2}{2r_1 r_2}\right) \end{aligned} \quad (9)$$

Similarly, the value of  $\gamma_2$ ,  $\mu_1$ , and  $\mu_2$  can be obtained.

From the above conclusions, it can be seen that there are 22 sets of solutions for the inverse kinematics of the parallel mechanism, that is, ‘+’ and ‘-’. The planar 3-DOF parallel mechanism under this configuration is named ‘+–’ mode. Similarly, the following four inverse assembly models can be obtained, as shown in Fig. 2.

### 3. GTW of redundant parallel mechanism

Aiming at the planar 6R parallel mechanism, the modern mathematical tool screw theory is used to define the motion/force transmission performance index in the DOF space of the parallel mechanism, so as to

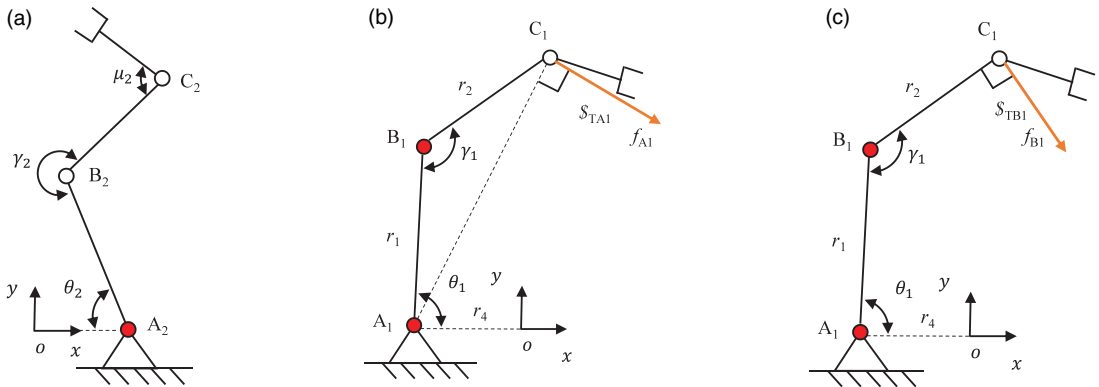


**Figure 3.** (a) RRR branched chain structure diagram, (b) joint  $A_1$  corresponding to the transfer wrench screw solution diagram, and (c) joint  $B_1$  corresponding to the transfer wrench screw solution diagram.

evaluate its performance. Based on the above research results, the kinematic performance evaluation rules suitable for planar 6R redundantly actuated parallel mechanisms are studied, and the identification method of GTW of mechanisms is explored.

### 3.1. Establishment of performance evaluation index

First, the twist screw and the wrench screw are solved. For the RRR (the underline indicates that this joint is the driving joint) branched chain, the structure diagram is shown in Fig. 3(a). In the RRR branch chain, there are three twist screw, which are as follows:

$$\begin{cases} \mathcal{S}_1 = (0, 0, 1; 0, -r_4, 0) \\ \mathcal{S}_2 = (0, 0, 1; r_1 \sin \theta_2, -r_4 - r_1 \cos \theta_2, 0) \\ \mathcal{S}_3 = (0, 0, 1; r_1 \sin \theta_2 + r_2 \sin(\gamma_2 - \theta_2), r_2 \cos(\gamma_2 - \theta_2) - r_4 - r_1 \cos \theta_2, 0) \end{cases} \quad (10)$$

These three twist screws can be used as a basis for the third-order screw system. There are three anti-screws, namely the number of constraint wrench screws, which are as follows:

$$\begin{cases} \mathcal{S}_1^r = (0, 0, 1; 0, 0, 0) \\ \mathcal{S}_2^r = (0, 0, 0; 1, 0, 0) \\ \mathcal{S}_3^r = (0, 0, 0; 0, 1, 0) \end{cases} \quad (11)$$

The transfer wrench screw represents  $B_2C_2$  pure force along the rod direction and passing through the center of the revolute joint  $B_2$  and  $C_2$ . The number of transfer wrench screws in a branch of the parallel mechanism is equal to the number of input joints. Assuming that the input joint  $A_2$  corresponding to the twist screw  $\mathcal{S}_1$  is locked, at least one new screw can be constructed. According to the concept of reciprocal product and the definition of the transfer wrench screw, the transfer wrench screw corresponding to the twist screw  $\mathcal{S}_1$  in the RRR branch chain can be obtained as follows:

$$\mathcal{S}_{TA2} = (-\cos(\gamma_2 - \theta_2), \sin(\gamma_2 - \theta_2), 0; 0, 0, r_4 \sin(\gamma_2 - \theta_2) + r_1 \sin \gamma_2) \quad (12)$$

For another RRR branched chain, the branched chain contains two input joints  $A_1$  and  $B_1$ , and its transfer wrench screw solution diagram is shown in Fig. 3(b). Assuming that the  $B_1$  joint is ‘locked’, the direction of the transmitted force of the input joint  $A_1$  is not along the direction of the rod  $B_1C_1$ , but along the direction perpendicular to the rod.

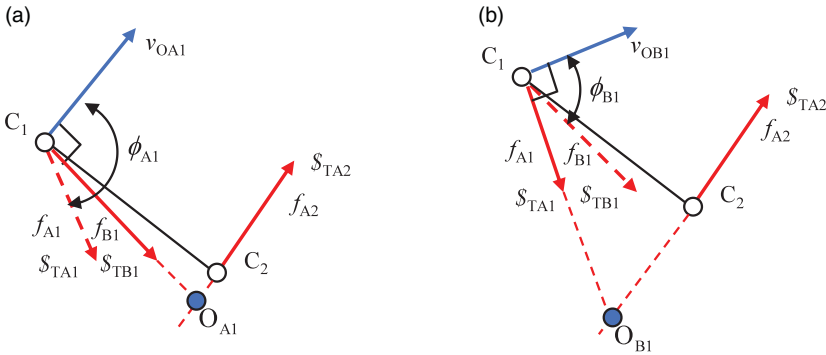


**Figure 4.** (a) Joint  $A_1$  corresponding to the output twist screw solution diagram and (b) joint  $B_1$  corresponding to the output twist screw solution diagram.

The transfer wrench screw corresponding to the joint in the branched RRR can be expressed as:

$$\mathcal{S}_{TA1} = (\mathbf{f}_{A1}; \mathbf{C}_1 \times \mathbf{f}_{A1}) \tag{13}$$

Among them:

$$\mathbf{f}_{A1} = \left( \frac{r_2 \sin(\gamma_1 + \theta_1) - r_1 \sin \theta_1}{\sqrt{r_1^2 + r_2^2 - 2r_1r_2 \cos \gamma_1}}, \frac{r_1 \cos \theta_1 - r_2 \cos(\gamma_1 + \theta_1)}{\sqrt{r_1^2 + r_2^2 - 2r_1r_2 \cos \gamma_1}}, 0 \right)$$

$$\mathbf{C}_1 \times \mathbf{f}_{A1} = \left( 0, 0, \frac{r_1^2 + r_2^2 - 2r_1r_2 \cos \gamma_1 - r_1r_2 \cos \theta_1 + r_2r_1 \cos(\gamma_1 + \theta_1)}{\sqrt{r_1^2 + r_2^2 - 2r_1r_2 \cos \gamma_1}} \right)$$

Similarly, the transfer wrench screw corresponding to the joint  $B_1$  in the branch RRR is shown in Fig. 3(c). The transfer wrench screw corresponding to the joint  $B_1$  can be expressed as:

$$\begin{aligned} \mathcal{S}_{TB1} &= (\mathbf{f}_{B1}; \mathbf{C}_1 \times \mathbf{f}_{B1}) \\ &= (\sin(\gamma_1 + \theta_1), -\cos(\gamma_1 + \theta_1), 0; 0, 0, r_4 \cos(\gamma_1 + \theta_1) + r_2 - r_1 \cos \gamma_1) \end{aligned} \tag{14}$$

Then the input and output twist screws are solved. The input twist screws of the planar 3-DOF 6R parallel mechanism correspond to their respective twist screws, which are as follows:

$$\begin{cases} \mathcal{S}_{IA1} = (0, 0, 1; 0, r_4, 0) \\ \mathcal{S}_{IB1} = (0, 0, 1; r_1 \sin \theta_1, r_4 - r_1 \cos \theta_1, 0) \\ \mathcal{S}_{IA2} = (0, 0, 1; 0, -r_4, 0) \end{cases} \tag{15}$$

The observation method is used to solve the output twist screw corresponding to joint  $A_1$  in the RRR branch. The schematic diagram of the solution process is shown in Fig. 4(a).

From the vector  $B_1C_1$ , the unit velocity vector of point  $C_1$  can be obtained as:

$$\mathbf{v}_{OA1} = (\cos(\gamma_1 + \theta_1), \sin(\gamma_1 + \theta_1), 0) \tag{16}$$

Therefore, the output twist screw  $\mathcal{S}_{OA1}$  is

$$\mathcal{S}_{OA1} = (\mathbf{v}_{OA1}; \mathbf{C}_1 \times \mathbf{v}_{OA1}) \tag{17}$$

Similarly, the solution process diagram of the output twist screw  $\mathcal{S}_{OB1}$  corresponding to the joint  $B_1$  in the RRR branched chain is shown in Fig. 4(b), and the output twist screw  $\mathcal{S}_{OB1}$  is

$$\mathcal{S}_{OB1} = (\mathbf{v}_{OB1}; \mathbf{C}_1 \times \mathbf{v}_{OB1}) \tag{18}$$

In the parallel mechanism, in order to make each transfer wrench screw to transfer the corresponding motion/force to the end effector well, the value of input transmission index (ITI) and output transmission

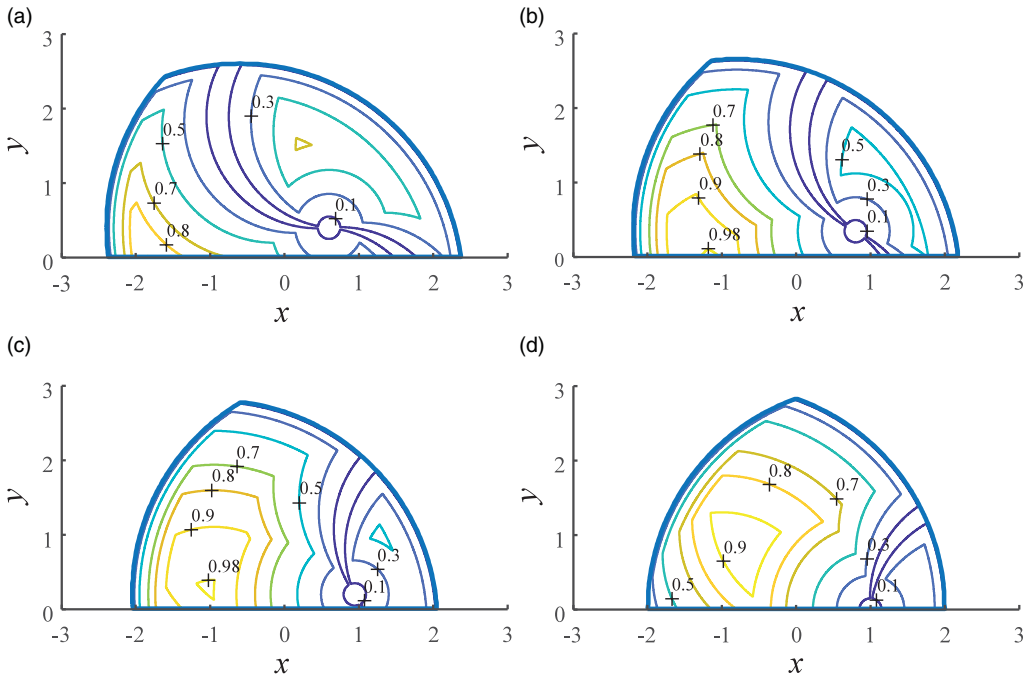


**Figure 5.** The distribution of LTI at different attitude angles: (a)  $\varphi = -\pi/2$ ; (b)  $\varphi = -2\pi/3$ ; (c)  $\varphi = -5\pi/6$ ; and (d)  $\varphi = -\pi$ .

index (OTI) is required to be close to 1. Therefore, this paper defines the local transmission index (LTI) of the institution as:

$$\begin{aligned} \gamma &= \min\{\gamma_1, \gamma_0\} = \min\{\lambda_1, \lambda_2, \lambda_3, \eta_1, \eta_2, \eta_3\} \\ &= \min\left\{|\sin \gamma_2|, \left|\frac{r_1 \sin \gamma_1}{\sqrt{r_1^2 + r_2^2 - 2r_1r_2 \cos \gamma_1}}\right|, |\sin \mu_2|\right\} \end{aligned} \tag{19}$$

The value range of  $\gamma$  is [0, 1].

The overall ITI of the organization is

$$\gamma_1 = \min_i\{\lambda_i\} = \min_i\left\{\frac{|\$T_i \circ \$I_i|}{|\$T_i \circ \$I_i|_{\max}}\right\} \quad (i = 1, 2, 3) \tag{20}$$

The overall OTI of the institution is

$$\gamma_0 = \min\{\eta_1, \eta_2, \eta_3\} = \min\left\{\left|\frac{r_1 \sin \gamma_1}{\sqrt{r_1^2 + r_2^2 - 2r_1r_2 \cos \gamma_1}}\right|, |\sin \mu_2|\right\} \tag{21}$$

Similarly, the dimensionless scale parameters of the parallel mechanism are  $r_1 = r_2 = 1.5, r_3 = 1.5,$  and  $r_4 = 0.6$ . The attitude angle range of the moving platform is  $(-\pi, -\pi/2)$ . The distribution of LTI in the fixed attitude workspace is shown in Fig. 5.

The distribution of LTI in the flexible workspace is shown in Fig. 6.

The solution result lays a theoretical foundation for the subsequent solution of the performance indexes of the redundantly driven parallel mechanism with singular configurations and GTW.

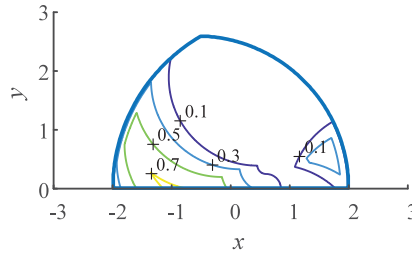


Figure 6. Distribution of LTI in flexible workspace.

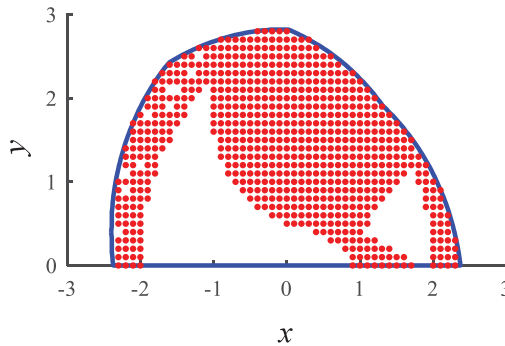


Figure 7. Singular workspaces in accessible workspaces.

### 3.2. Mechanism singularity analysis

Glazunov *et al.* [25] proposed a singularity determination criterion based on the mathematical relationship between the input/output twist screw and the transfer wrench screw. In this paper, with reference to the above method, the following two singularities are defined: when the input transmission index (ITI) is equal to 0, the motion/force corresponding to the input joints cannot be transferred out, which is called input transmission singularity (ITS). Similarly, defining the output transmission singularity (OTS):

$$\begin{aligned}
 \text{ITS} &= \min_i \{ |\$T_i \circ \$i| \} \rightarrow 0, (i = 1, 2, 3) \\
 \text{OTS} &= \min_i \{ |\$T_i \circ \$O_i| \} \rightarrow 0, (i = 1, 2, 3)
 \end{aligned}
 \tag{22}$$

The dimensionless scale parameters of the parallel mechanism are taken as  $r_1 = r_2 = 1.5$ ,  $r_3 = 0.4$ , and  $r_4 = 0.6$ , and the attitude angle range of the moving platform is  $(-\pi, -\pi/2)$ . The transfer singular workspace of the mechanism in the reachable workspace is shown in Fig. 7.

The area formed by the red scattering points represents the transfer singular workspace of the parallel mechanism under the reachable workspace. When the reference point of the end-moving platform of the mechanism is at (0.5, 2), (1.5, 2), (0.5, 1), and (1.5, 1), the variation of the LTI of the mechanism with the end attitude angle is shown in Fig. 8:

When the reference point of the moving platform at the end of the mechanism is rotated at (0.5, 2), (1.5, 2), and (0.5, 1), the value of LTI is equal to 0 at  $\varphi = -132^\circ$ ,  $\varphi = -156^\circ$ ,  $\varphi = -136^\circ$ , respectively, which indicates that the mechanism is in the passing singular configuration under this configuration. At this time, the possible singular position of the mechanism is shown in Fig. 9:

Applying ITS and OTS to singularity analysis of planar parallel mechanisms without solving their Jacobi matrices and being able to identify all types of singularity of the mechanism (ITS and OTS) reveals the nature of singularity occurring in the mechanism and similarly can be obtained for the singular configuration under the other combinations of non-redundantly driven joints



**Table I.** 18 Non-redundant parallel mechanisms.

Including joints	Driving joint		
$A_1B_1$	$A_1B_1C_2$	$A_1B_1B_2$	$A_1B_1C_2$
$A_1C_1$	$A_1C_1A_2$	$A_1C_1B_2$	$A_1C_1C_2$
$A_1A_2$	$A_1A_2B_2$	$A_1A_2C_2$	—
$A_1B_2$	$A_1B_2C_2$	—	—
$B_1C_1$	$B_1C_1A_2$	$B_1C_1B_2$	$B_1C_1C_2$
$B_1A_2$	$B_1A_2B_2$	$B_1A_2C_2$	—
$B_1B_2$	$B_1B_2C_2$	—	—
$C_1A_2$	$C_1A_2B_2$	$C_1A_2C_2$	—
$C_1B_2$	$C_1B_2C_2$	—	—

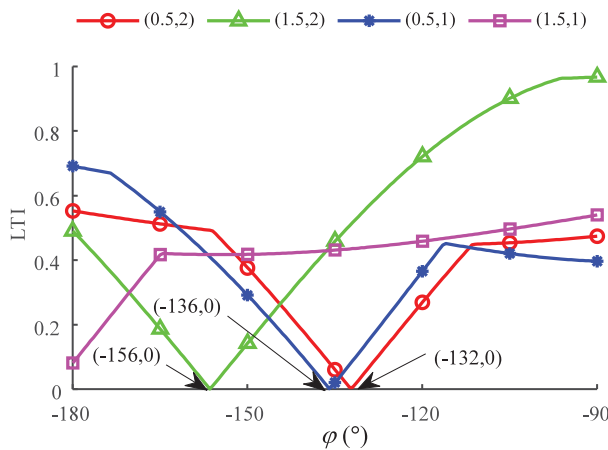


**Figure 8.** Variation of mechanism LTI with end attitude angle.

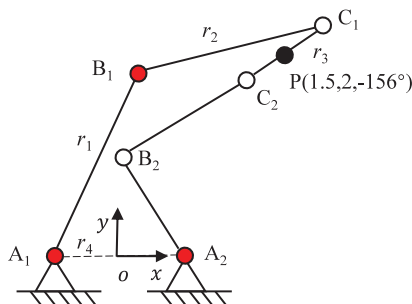


**Figure 9.** Parallel mechanism transmits singular configuration.

**3.3. Motion/force transmission performance analysis of non-redundant parallel mechanism**

The planar 3-DOF 6R parallel mechanism is an asymmetric mechanism. Three joints are randomly selected from the six driving joints as the driving joints, and 20 non-redundant parallel mechanisms are obtained. The joints  $A_1, B_1, C_1$  and joints  $A_2, B_2, C_2$  are removed as the driving parallel mechanisms. The remaining 18 non-redundant parallel mechanisms are shown in Table I.

When there is  $A_1$  joint, the parallel mechanism has a total of nine non-redundant forms, among which the non-redundant form driven by  $A_1B_1A_2$  has been analyzed in detail. The motion/force transmission indexes of the remaining eight non-redundant forms and the non-redundant parallel mechanism with  $A_1$  joint under each driving mode are shown in Table II.

**Table II.** Contains the motion/force transmission index of  $A_1$  joint under each driving mode.

Driving joint	Drive mode	LTI
$A_1B_1C_2$		$LTI_{A_1B_1C_2} = \min\left\{1, 1,  \sin \gamma_2 , \left \frac{r_1}{A_1C_1} \sin \gamma_1\right , \left \frac{r_1}{A_1C_1} \sin \gamma_1\right ,  \sin \alpha_1 \right\}$
$A_1C_1A_2$		$LTI_{A_1C_1A_2} = \min\{1, 1,  \sin \gamma_2 ,  \cos \alpha_1 ,  \cos \alpha_2 ,  \sin \alpha_3 \}$
$A_1C_1B_2$		$LTI_{A_1C_1B_2} = \min\{1, 1,  \sin \gamma_2 ,  \cos \alpha_1 ,  \cos \alpha_2 ,  \sin \alpha_3 \}$

Table II. Continued.

Driving joint	Drive mode	LTI
$A_1C_1C_2$		$LTI_{A_1C_1C_2} = \min\{1, 1,  \sin \gamma_2 ,  \cos \alpha_1 ,  \cos \alpha_2 ,  \cos \alpha_3 \}$
$A_1A_2B_2$		$LTI_{A_1A_2B_2} = \min\left\{ \sin \gamma_1 , 1, 1,  \sin \mu_1 , \left \frac{r_1}{A_2C_2} \sin \gamma_2\right , \left \frac{r_1}{A_2C_2} \sin \gamma_2\right \right\}$
$A_1A_2C_2$		$LTI_{A_1A_2C_2} = \min\{ \sin \gamma_1 , 1, 1,  \sin \alpha_1 ,  \cos \alpha_2 ,  \cos \alpha_3 \}$
$A_1B_2C_2$		$LTI_{A_1B_2C_2} = \min\{ \sin \gamma_1 , 1, 1,  \sin \alpha_1 ,  \cos \alpha_2 ,  \cos \alpha_3 \}$

In addition to the above non-redundant parallel mechanism with  $A_1$  joint, the motion/force transmission indexes of the non-redundant parallel mechanism with  $B_1$  joint under each driving mode are shown in Table III.

In addition to the above non-redundant parallel mechanisms with  $A_1$  and  $B_1$  joints, there are three non-redundant forms of the parallel mechanism with  $C_1$  joints, as shown in Table IV.

### 3.4. GTW identification of redundantly actuated parallel mechanisms

For the drive redundant parallel mechanism, the Local Minimized Transmission Index (LMTI) is used to evaluate the motion/force transmission performance of the drive redundant parallel mechanism.

Assuming that the driving number of the mechanism is  $k$  and the redundancy is  $r$ , this paper makes the redundant driving joints follow up, and then  $q$  non-redundant parallel mechanisms can be obtained, that is,  $q = C_k^r$ . According to the definition of LTI in Eq. (19), when the end-moving platform of the parallel mechanism is in any position, there must be a non-redundant parallel mechanism, and its LTI value is better than that of other non-redundant parallel mechanisms. The LTI value is the local minimum transmission index of the driving redundant parallel mechanism. It can be described as follows:

$$\text{LMTI} = \max\{\varepsilon_1, \varepsilon_2, \dots, \varepsilon_q\} \quad (q = C_k^r) \quad (23)$$

where  $\varepsilon$  represents the institution's LTI.

The LMTI value of the mechanism is in the range of [0,1]. The distribution of LMTI of the redundantly actuated parallel mechanism at different attitude angles is shown in Fig. 10.

The distribution of the LMTI in the flexible workspace of the mechanism in a specific angle range is shown in Fig. 11.

Compared with the  $A_1B_2A_1$  joint drive, the motion/force transmission performance of the mechanism is significantly improved by introducing the full-redundant drive mode in the flexible workspace of the fixed attitude. Therefore, the planar 3-DOF 6R parallel mechanism in this paper is driven by full redundancy to improve the overall kinematic performance of the mechanism.

If the attitude of the moving platform is given, the area with LTI (LMTI)  $\geq 0.7$  is defined as GTW. The distribution of GTW in the flexible workspace of the mechanism is shown in Fig. 12 under the full-redundant drive and the specific angle range.

Compared with the area of LTI  $\geq 0.7$  in the flexible workspace under the non-redundant driving mode shown in Fig. 6, the area of the GTW of the mechanism under the fully redundant driving mode increases by 5.45, and the growth amplitude reaches 136 times. Similarly, according to the definition of singularity, it is found that there is no singularity configuration in the 6R parallel mechanism under the full-redundant driving mode, and its kinematic performance is greatly improved.

## 4. Dimension optimization of redundantly actuated parallel mechanism

In this section, the dimension of the planar 6R mechanism is dimensionless and the parameter design space is established by using the space model theory. Then, the mapping relationship between the workspace shape, area, motion/force transmission performance index, and scale of the redundantly actuated parallel mechanism is established, and the performance map is drawn. Finally, based on the performance map, the optimization design of the mechanism scale is completed from a global perspective.

### 4.1. Dimensionless method and parameter design space

It can be seen from Fig. 1 that there are four scale variables in the planar 6R parallel mechanism, and each member is dimensionless. Let:

$$\begin{cases} r_i = R_i/L \\ L = \frac{1}{4} \sum_{i=1}^4 R_i \end{cases}, (i = 1, 2, 3, 4) \quad (24)$$

**Table III.** Contains the motion/force transmission index of  $B_1$  joint under each driving mode.

Driving joint	Drive mode	LTI
$B_1C_1A_2$		$LTI_{B_1C_1A_2} = \min\{1, 1,  \sin \gamma_2 ,  \cos \alpha_1 ,  \cos \alpha_2 ,  \sin \alpha_3 \}$
$B_1C_1B_2$		$LTI_{B_1C_1B_2} = \min\{1, 1,  \sin \gamma_2 ,  \cos \alpha_1 ,  \cos \alpha_2 ,  \sin \alpha_3 \}$
$B_1C_1C_2$		$LTI_{B_1C_1C_2} = \min\{1, 1,  \sin \gamma_2 ,  \cos \alpha_1 ,  \cos \alpha_2 ,  \sin \alpha_3 \}$
$B_1A_2B_2$		$LTI_{B_1A_2B_2} = \min\left\{ \sin \gamma_1 , 1, 1,  \sin \alpha_1 , \left \frac{r_1}{A_2C_2} \sin \gamma_2\right , \left \frac{r_1}{A_2C_2} \sin \gamma_2\right \right\}$

Table III. Continued.

Driving joint	Drive mode	LTI
$B_1A_2C_2$		$LTI_{B_1A_2C_2} = \min\{ \sin \gamma_1 , 1, 1,  \sin \alpha_1 ,  \cos \alpha_2 ,  \cos \alpha_3 \}$
$B_1B_2C_2$		$LTI_{B_1B_2C_2} = \min\{ \sin \gamma_1 , 1, 1,  \sin \alpha_1 ,  \cos \alpha_2 ,  \cos \alpha_3 \}$

where  $R_i$  and  $r_i$  denote the actual length and dimensionless parameters of the member, respectively, then:

$$r_1 + r_2 + r_3 + r_4 = 4 \tag{25}$$

According to the structural characteristics and assembly constraints of the robot, it can be obtained:

$$\begin{cases} 0 < r_1, r_2 < 4 \\ 0 < r_3, r_4 < 2 \end{cases} \tag{26}$$

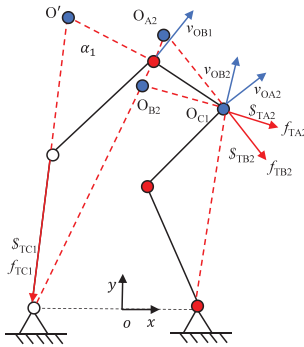
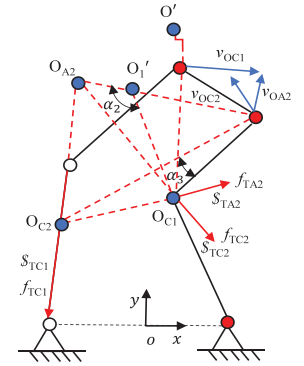
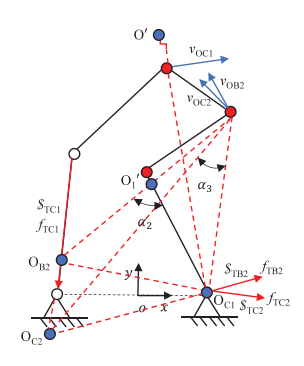
The spatial model of the mechanism is shown in Fig. 13(a).

We are accustomed to using the plane coordinate system  $o' - xy$  instead of the dimensionless coordinates, so we can get the spatial model plane diagram as shown in Fig. 13(b).

The conversion relationship of the coordinate system is

$$\begin{cases} x = \frac{2\sqrt{3}}{3}r_1 + \frac{\sqrt{3}}{3}r_3 \\ y = r_3 \end{cases} \tag{27}$$

**Table IV.** Contains the motion/force transmission index of  $C_1$  joint in each driving mode.

Driving joint	Drive mode	LTI
$C_1A_2B_2$		$LTI_{C_1A_2B_2} = \min\left\{  \sin \gamma_1 , 1, 1,  \sin \alpha_1 , \left  \frac{r_1}{A_2C_2} \sin \gamma_2 \right , \left  \frac{r_1}{A_2C_2} \sin \gamma_2 \right  \right\}$
$C_1A_2C_2$		$LTI_{C_1A_2C_2} = \min\{  \sin \gamma_1 , 1, 1,  \sin \alpha_1 ,  \cos \alpha_2 ,  \cos \alpha_3  \}$
$C_1B_2C_2$		$LTI_{C_1B_2C_2} = \min\{  \sin \gamma_1 , 1, 1,  \sin \alpha_1 ,  \cos \alpha_2 ,  \cos \alpha_3  \}$

In this section, the space model plan of the mechanism is established through the constraints and assembly conditions of the parallel mechanism, which provides an effective tool for the subsequent scale optimization design.

#### 4.2. Dimension optimization design of parallel mechanism

In each plane diagram of the spatial model of the planar 3-DOF 6R parallel mechanism, six straight lines can be divided into several small intervals, and the area and shape of the workspace of the parallel mechanism can be studied according to the different scale characteristics in each interval.

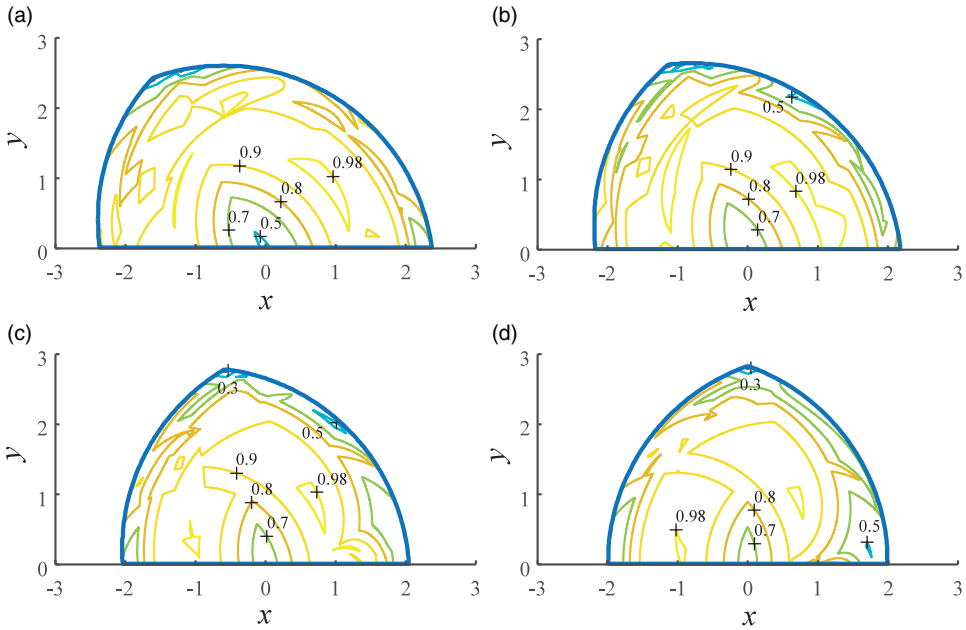


**Figure 10.** The distribution map of LMTI at different attitude angles: (a)  $\varphi = -\pi/2$ ; (b)  $\varphi = -2\pi/3$ ; (c)  $\varphi = -5\pi/6$ ; and (d)  $\varphi = -\pi$ .

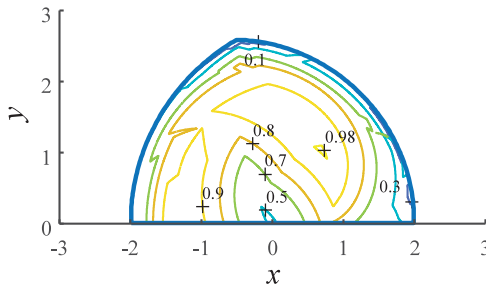


**Figure 11.** Distribution of LMTI in flexible workspace.

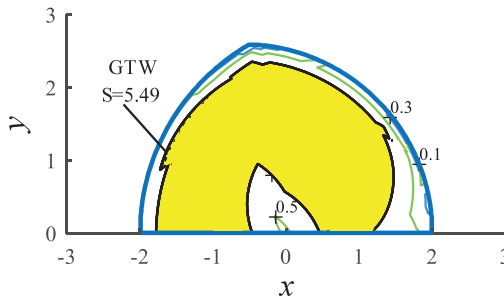


**Figure 12.** The GTW distribution diagram of the mechanism under the full-redundant driving mode.

When  $0 < r_4 < 1$ , the plane interval diagram of the space model is shown in Fig. 14.

The range of the attitude angle of the end is  $(-\pi, -\pi/2)$ . According to the workflow solution process, when  $0 < r_4 < 1$ , the mapping relationship between the shape and scale of the workspace is shown in Fig. 15. Similarly, the mapping relationship between the shape and scale of the workspace under the remaining scales can be obtained.



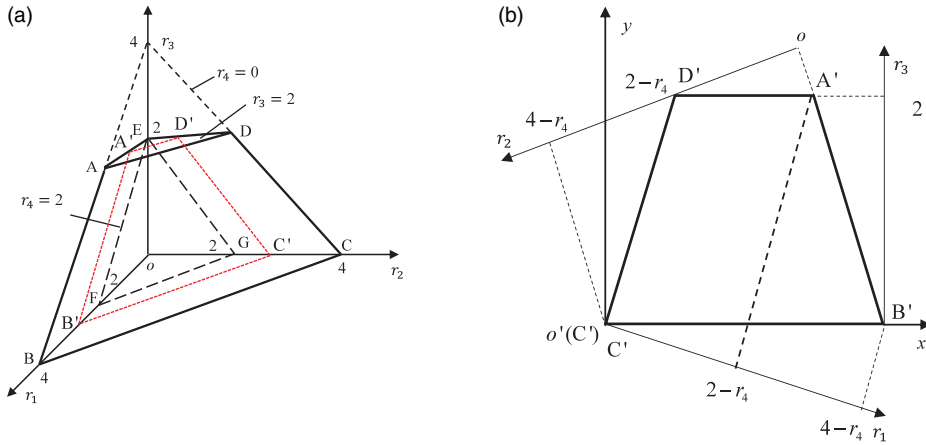


**Figure 13.** The spatial model of the mechanism: (a) space model of parallel mechanism and (b) plane diagram of space model.

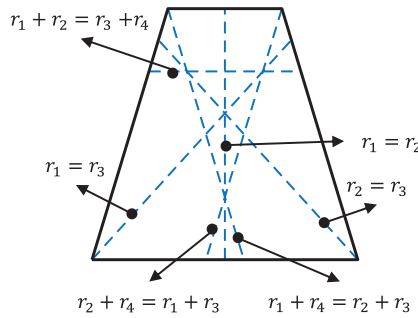


**Figure 14.** Plane interval diagram of space model ( $0 < r_4 < 1$ ).

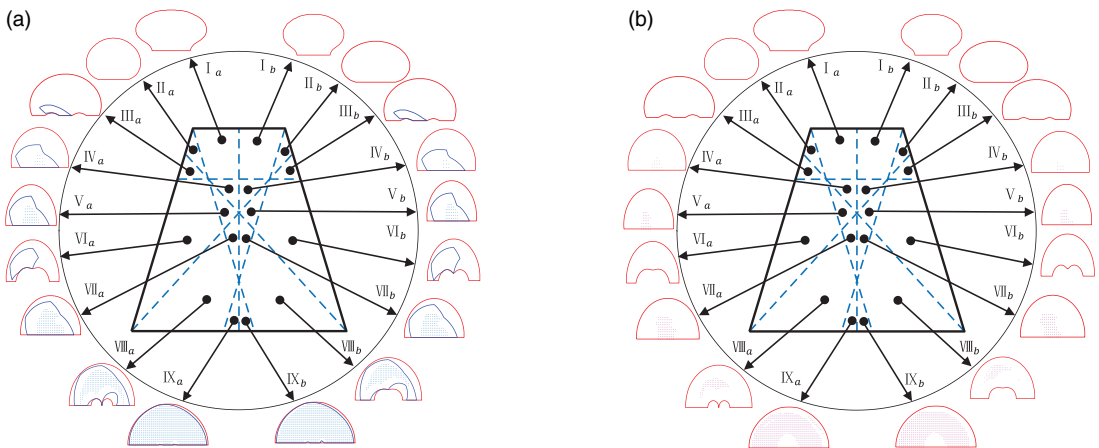


**Figure 15.** Mapping relationship between the shape and scale of the workspace: (a) mapping relationship between shape and scale of reachable/flexible workspace and (b) mapping relationship between shape and scale of good transmission workspace.

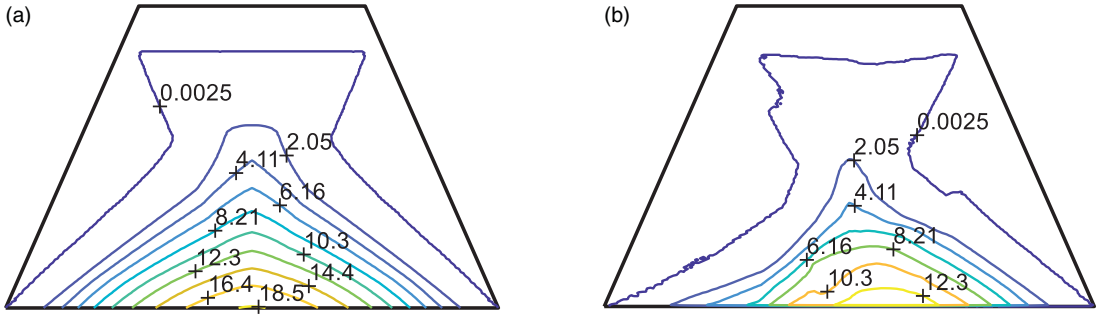


**Figure 16.** Mapping relationship between workspace area and scale: (a) mapping relationship between reachable/flexible workspace area and scale and (b) mapping relationship between good transmission workspace area and scale.

The distribution of the workspace area in the design space cannot be understood from the above map. The number of points searched under a certain step size is used as the evaluation index of the workspace value (WSV). While searching the flexible workspace of the parallel mechanism, the area of the workspace can be calculated. Taking  $r_4 = 0.3$  as an example, as shown in Fig. 16, the mapping relationship at other scales can be obtained.

In summary, the planar 6R parallel mechanism achieves a large area in order to obtain the reachable/flexible workspace and the GTW based on it under a specific rotation angle range  $(-\pi, -\pi/2)$ , the smaller the  $r_4$  is, the better. The value range of  $r_4$  is specified as  $(0, 1]$ . At this time, the scale range of the parallel mechanism should be selected as:

$$\begin{cases} r_1 + r_4 > r_2 + r_3 \\ r_2 + r_4 > r_1 + r_3 \end{cases} \quad (28)$$

Since the performance of the mechanism is different under different poses at the same scale, and there is no constraint performance evaluation problem in the planar 3-DOF 6R parallel mechanism, this paper defines

$$\Lambda = \min\{\gamma\} = \min\{\gamma_1, \gamma_0\} \quad (29)$$

$\Lambda$  represents the local design index (LDI). The set of all pose points with  $\text{LDI} \geq 0.7$  is defined as the GTW of the mechanism. The obtained area is a global index for the scale optimization design of the parallel mechanism. The average value of the LDI of the defined mechanism in the GTW is

$$\Gamma = \frac{\int_w \Lambda dw}{\int_w dw} \quad (30)$$

where  $\Gamma$  represents the GTI and  $w$  represents the organization's GTW.

Taking  $r_4 = 0.3$  as an example, the mapping relationship between the global transmission index and the scale of the parallel mechanism is obtained as shown in Fig. 17.

The analysis shows that the planar 3-DOF 6R parallel mechanism should select the scale in the area with higher global transmission index value under the specific rotation angle range  $(-\pi, -\pi/2)$ , so as to obtain better overall performance.

In conjunction with Fig. 16(b), the optimized area of the parallel mechanism within the parametric design space is shown in Fig. 18. The area enclosed by the solid blue line and the solid red line in the figure represents the range of the global transmission index value of the institution greater than 0.87 and the range of the GTW area of the institution when  $= 0.3$ , respectively, and the green intersection area of the two is the optimization area in the parameter design space, and the optimization area under the rest of the scales can be obtained by the same reason. The combination of institutional scales in the preferred scale area meets the design requirements, and the GTW area of the formed mechanism is

**Table V.** Size parameters of 6R mechanism.

$R_1/m$	$R_2/m$	$R_3/m$	$R_4/m$
1.2	1.2	0.3	0.66

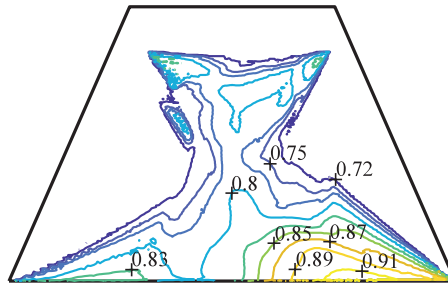


**Figure 17.** Mapping relationship between global transmission index and scale of parallel mechanism.

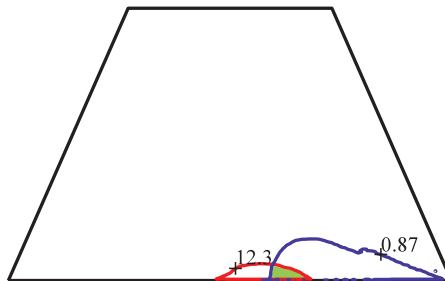


**Figure 18.** Optimization region of parallel mechanism in parameter design space.

relatively large, and the value of the institutional GTI is above 0.87, which proves the correctness of the theory and method of institutional scale optimization.

### 5. Prototype production and performance verification

In this part, the scale parameters of the key components of the mechanism are selected, the good task space of the robot is analyzed, and the dynamic model of the mechanism is established. Finally, the control strategy analysis and prototype performance verification are carried out.

#### 5.1. Scale selection and task space analysis

The redundantly actuated parallel robot requires 6 DOF, so the robot system is composed of a planar 3-DOF 6R mechanism as the main functional component, combined with the rotation of the waist and the end wrist that can rotate around the  $x$  and  $y$  axes, respectively. Taking into account the results of component interference and assembly constraints and scale optimization, the scale parameters selected in the high-quality scale domain are shown in Table V.

The redundantly actuated parallel robot system designed in this paper is shown in Fig. 19.

In the process of robot operation, its task space is a regular geometry. Therefore, it is necessary to properly deal with the irregular geometry when determining the good task space of the mechanism.

Combined with the operation process of the robot, this paper assumes that the attitude angle range of the moving platform at the end of the parallel mechanism is  $(-\pi, -\pi/2)$ , and then when the scale



**Figure 19.** Main structure prototype of redundantly actuated parallel robot.

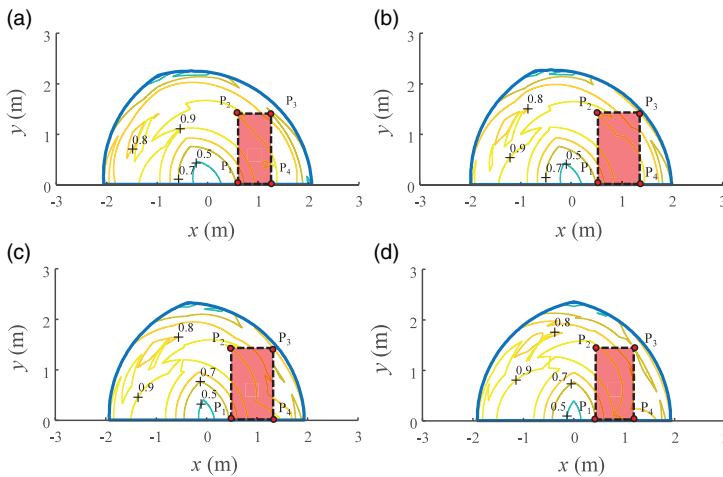


**Figure 20.** Good task space of the mechanism under different attitude angle: (a)  $\varphi = -\pi/2$ ; (b)  $\varphi = -2\pi/3$ ; (c)  $\varphi = -5\pi/6$ ; and (d)  $\varphi = -\pi$ .

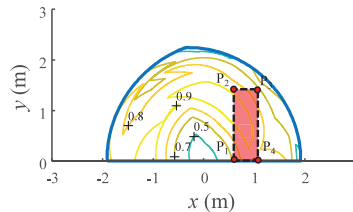


**Figure 21.** Good task space of parallel mechanism in flexible workspace.

parameters of the parallel mechanism are  $R_1 = R_2 = 1.2$  m,  $R_3 = 0.3$  m, and  $R_4 = 0.66$  m, the good task space of the mechanism in the fixed attitude workspace is shown in Fig. 20.

Similarly, the spatial distribution of good tasks in the flexible workspace of the mechanism within a specific angle range is shown in Fig. 21.

In order to make the robot have a large good task space and complete the handling, loading, and unloading of large-mass components on the side of the robot, this paper defines the good task space of the redundantly actuated parallel robot as a rectangular area surrounded by the dotted line in Fig. 20 and Fig. 21.

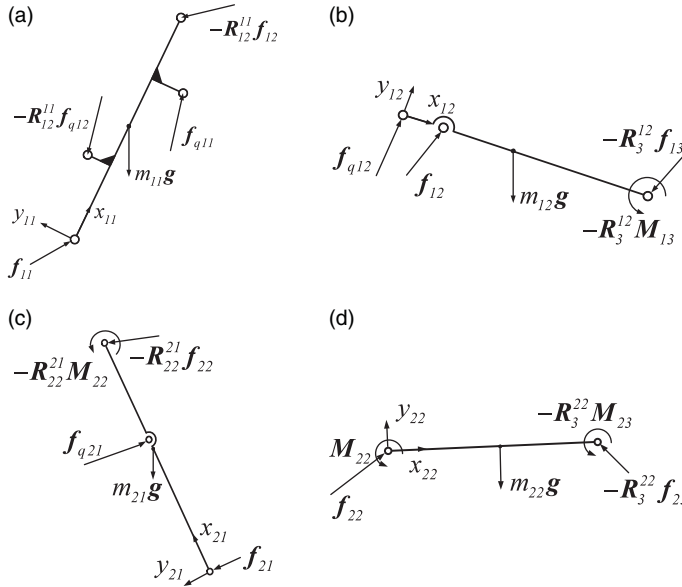


Figure 22. The free-body diagram of each structural member in branch chains.

5.2. Dynamics analysis of redundant drive parallel mechanism

Before conducting research on robotic arm control, its dynamics need to be modeled. The Newton–Euler method is employed to establish the dynamic model for this mechanism. In order to facilitate the dynamic formulation, a local coordinate frame is established at the onset of each structural member, as depicted in Fig. 22. All subsequent dynamics calculations are performed within this local coordinate frame.

The acceleration of the center of mass for bar  $ij$  and the end for bar  $ij$  can be expressed by the following equation:

$$\begin{aligned}
 \mathbf{a}_{c,ij} &= (\mathbf{R}_{ij}^{i(j-1)})^T \mathbf{a}_{e,i(j-1)} + \dot{\mathbf{w}}_{ij} \times \mathbf{r}_{ij,c} + \mathbf{w}_{ij} \times (\mathbf{w}_{ij} \times \mathbf{r}_{ij,c}), \quad i, j = 1, 2 \\
 \mathbf{a}_{e,ij} &= (\mathbf{R}_{ij}^{i(j-1)})^T \mathbf{a}_{e,i(j-1)} + \dot{\mathbf{w}}_{ij} \times \mathbf{r}_{ij,i(j+1)} + \mathbf{w}_{ij} \times (\mathbf{w}_{ij} \times \mathbf{r}_{ij,i(j+1)}), \quad i, j = 1, 2
 \end{aligned}
 \tag{31}$$

The gravity acceleration (expressed in frame  $ij$ ) can be expressed as:

$$\mathbf{g}_{ij} = (\mathbf{R}_{ij})^T \mathbf{g}, \quad i, j = 1, 2
 \tag{32}$$

The parallel mechanism consists of an upper branch and a lower branch, where  $i$  represents the upper branch or the lower branch of the mechanism, the upper branch when  $i = 1$  and the lower branch when  $i = 2, j$  determine a bar in the branch chain, where  $j = 1$  represents the bar connected to the fixed base in the branch chain and  $j = 2$  represents the bar connected to the moving platform in the branch chain.  $\mathbf{R}_{ij}$  is the rotation matrix from frame  $ij$  to fixed frame.  $\mathbf{R}_{ij}^{i(j-1)}$  is the rotation matrix from frame  $ij$  to frame  $i(j-1)$ . Eq. (31), when  $i = 1$  and  $j = 1$ , represents the linear acceleration of a coordinate system attached to a fixed platform, so  $\mathbf{a}_{e,i(j-1)} = 0$ .  $\mathbf{w}_{ij}$  is the angular velocity of bar  $ij$  in frame  $ij$ ,  $\mathbf{r}_{ij,c}$  is the vector from joint  $ij$  to the center of mass of bar  $ij$ ,  $\mathbf{r}_{ij,i(j+1)}$  is the vector from joint  $ij$  to joint  $i(j+1)$ ,  $\mathbf{g}$  is gravity acceleration from fixed frame.

The force balance and moment balance equation for bar  $ij$  can be expressed by Eq. (33).

$$\begin{cases}
 \mathbf{f}_{ij} - \mathbf{R}_{i(j+1)}^{ij} \mathbf{f}_{i(j+1)} + m_{ij} \mathbf{g}_{ij} = m_{ij} \mathbf{a}_{c,ij} \\
 \boldsymbol{\tau}_{ij} - \mathbf{R}_{i(j+1)}^{ij} \boldsymbol{\tau}_{i(j+1)} + \mathbf{f}_{ij} \times \mathbf{r}_{ij,c} - (\mathbf{R}_{i(j+1)}^{ij} \mathbf{f}_{i(j+1)}) \times \mathbf{r}_{i(j+1),c}, \quad i, j = 1, 2 \\
 = I_{ij} \dot{\boldsymbol{\omega}}_{ij} + \boldsymbol{\omega}_{ij} \times I_{ij} \boldsymbol{\omega}_{ij}
 \end{cases}
 \tag{33}$$

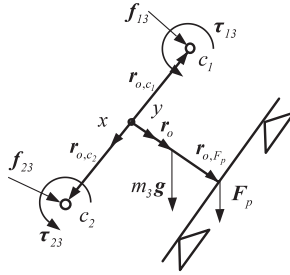


Figure 23. The free-body diagram of moving platform.

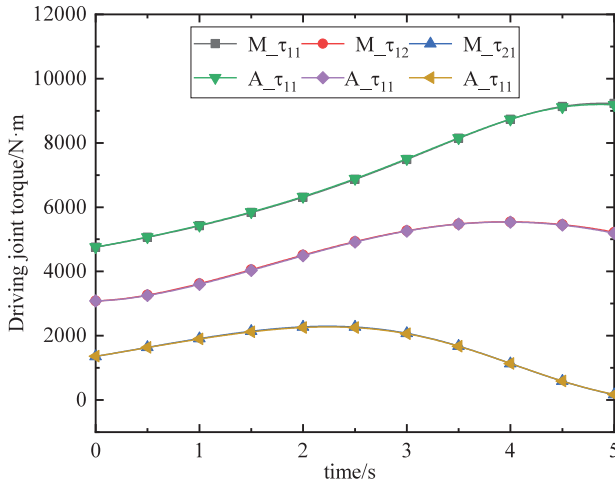


Figure 24. Comparison of drive torque calculation and simulation.

where  $f_{ij}$  is the force exerted by bar  $i(j - 1)$  on bar  $j$ ,  $\tau_{ij}$  is the torque exerted by bar  $i(j - 1)$  on bar  $j$ ,  $m_{ij}$  is the mass of bar  $j$ , and  $I_{ij}$  is the inertia matrix of bar  $ij$  evaluated at a frame parallel to frame  $ij$  located at the center of mass. The forces and moments applied to the moving platform are shown in Fig. 23.

In order to analyze the moving platform more effectively, the force balance equation and the moment balance equation of the moving platform are established as follows:

$$\begin{cases} f_{13} + f_{23} + F_p + m_3g = m_3\ddot{x}_p\mathbf{i} + m_3\ddot{y}_p\mathbf{j} \\ \tau_{13} + \tau_{23} + f_{13} \times (-r_{o,C_1} + r_o) + f_{23} \times (-r_{o,C_2} + r_o) + F_p \times (-r_{o,F_p} + r_o) \\ = I_3\ddot{\varphi}_p\mathbf{k} \end{cases} \quad (34)$$

Based on Eq. (33) and Eq. (34), the dynamic equation of the mechanism can be transformed into the following form:

$$A_F \tau = B \quad (35)$$

where  $A_F \in \mathbf{R}^{3 \times 6}$ ,  $\tau = [\tau_{11} \ \tau_{11} \ \tau_{11} \ \tau_{11} \ \tau_{11} \ \tau_{11}]^T$ .

Dynamics modeling is done, and dynamics simulation is done using Adams. The moving platform moves from a point with coordinates  $(1.15, 0.429, -\pi)$  to another point with coordinates  $(1.4, 1.9, -\pi/2)$ . In order to avoid the influence of a specific trajectory on the simulation results, three trajectories are taken between the two points. The moving platform is rotated 90 degrees counterclockwise at a constant speed in 10 s. The calculated and simulated results of the driving torque are shown in Fig. 24, which verifies the correctness of the dynamics model established in this paper and lays a theoretical foundation for the research of the control strategy.

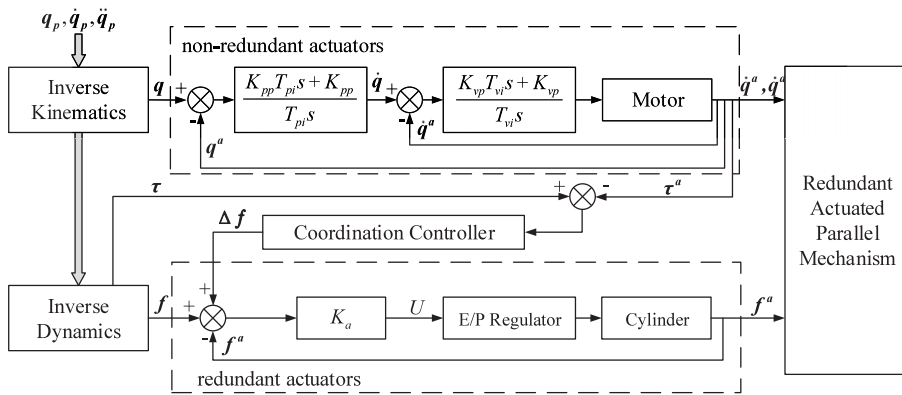


Figure 25. Control scheme for redundant drive parallel mechanism.

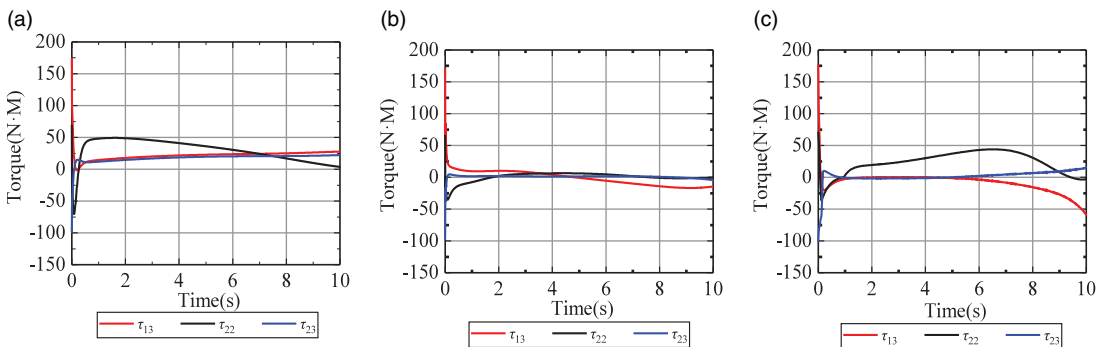


Figure 26. Motor torque of force–position hybrid coordinated control.

### 5.3. Research on control strategy of redundant drive parallel mechanism

In this paper, a force–position hybrid control strategy is used for simultaneous force and position control, and redundant and non-redundant actuators are used for force and position control, respectively [26–27]. The non-redundant joints of the mechanism are driven by three servo motors, which act as position controllers. The redundant actuator consists of three sets of cylinders that act as force controllers and take the responsibility of supporting the mechanism’s self-weight and external loads. This scheme has problems in application such as discrepancies between the theoretical and practical systems and poor synchronization between the actuators. In order to solve these problems, a coordination controller is used in this study to take the real-time output torque from the servomotors as input and calculate the force adjustment value of the cylinders through error coupling operation, which in turn corrects the output force of the cylinders.

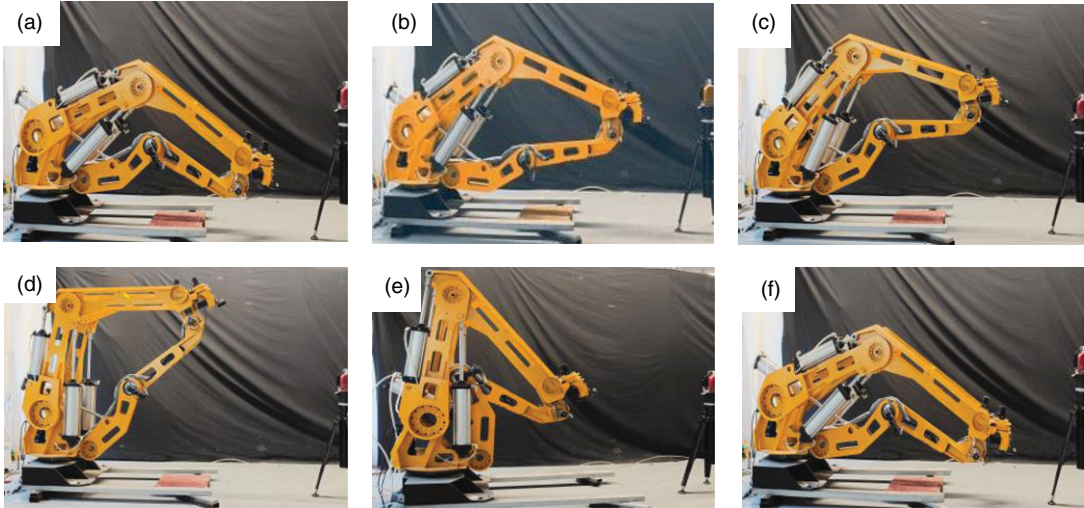
The control scheme of the redundant drive parallel mechanism is shown in Fig. 25.  $q_p$ ,  $\dot{q}_p$ , and  $\ddot{q}_p$  are the desired position, velocity, and acceleration of the moving platform, respectively. The expected output force of the cylinder and the expected rotation angle of the motor can be calculated.  $\tau$  represents the desired torque of the motor with a value of 0.  $\tau^a$  represents the actual torque of the motor, and  $\Delta f$  represents the adjustment of the cylinder based on the error of the motor torque.

The moving platform moves from a point with coordinates (1.15, 0.429,  $-\pi$ ) to another point with coordinates (1.4, 1.9,  $-\pi/2$ ), and three kinds of trajectories are randomly selected between the two points, and the motor angle and motor torque are calculated for the two kinds of motion trajectories under no-load conditions. The motor torque of force–position hybrid coordinated control is shown in Fig. 26.



**Table VI.** Redundant drive parallel robot position repeatability measurement points coordinates.

$W_1/\text{mm}$	$W_2/\text{mm}$	$W_3/\text{mm}$	$W_4/\text{mm}$	$W_5/\text{mm}$
(1385,655)	(1255,955)	(1155,1055)	(855,830)	(1385,655)

**Figure 27.** Position repeatability test of redundantly actuated parallel robot.

It can be seen that the advantages of this mechanism are obvious, dramatically reducing the torque required for unknown control of the joints, which allows the robot to use less powerful motors to achieve precise position control, thus reducing the overall weight of the robot.

#### 5.4. Performance verification experiments for redundantly driven parallel robots

The load to weight ratio is defined as:

$$\eta = \frac{m_{\max}}{M} \times 100\% \quad (36)$$

In Eq. (36),  $m_{\max}$  represents the maximum load of the robot and  $M$  represents the mass of the robot.

The experimental results showed that  $m_{\max} = 120$  kg and  $M = 758$  kg. According to Eq. (36), the load-to-weight ratio of the redundantly actuated parallel robot developed in this paper is 15.83 %. The calculation results show that the redundantly actuated parallel robot designed in this paper can be competent for the installation task under the requirement of large load.

In order to detect the position repeatability and position accuracy of the robot, five measurement points are randomly selected in the good task space shown in Fig. 20 and Fig. 21. The coordinates of the five measurement points in the workspace are shown in Table VI.

Maneuvering robot executes  $W_1$  point,  $W_2$  point,  $W_3$  point,  $W_4$  point, and  $W_5$  point sequentially from  $W_5$  point and repeats 30 times. In the process of executing the pose point of the robot, the API-RADIAN laser tracker is used to measure and record the pose information of the robot end effector when executing  $W_1$ ,  $W_2$ ,  $W_3$ ,  $W_4$ , and  $W_5$ . Fig. 27 is a scene photo of the redundantly actuated parallel robot performing pose point detection.

A set of coordinate points obtained by multiple measurements of the same measurement point using a laser tracker can be used to construct a circumscribed sphere that envelopes the three-dimensional



**Table VII.** Position repeatability parameters of redundantly actuated parallel robot at each measurement point.

Measuring point/mm	$W_1$	$W_2$	$W_3$	$W_4$	$W_5$
Repeatability errors/mm	0.042	0.048	0.053	0.041	0.049
Position accuracy/mm	0.520	0.510	0.570	0.635	0.565

**Table VIII.** Performance parameters of redundantly actuated parallel robots under different loads.

Load weight/kg	Repeatability of position/mm	Position accuracy/mm
10	0.060	0.646
20	0.065	0.655
30	0.069	0.692
40	0.072	0.715
50	0.078	0.720
60	0.079	0.733

coordinates of all measured points. The radius RP1 of the constructed circumscribed sphere is the position repeatability of the robot end effector, which is also called the position repeatability of the robot. By processing the measurement results of the redundantly actuated parallel robot, the position repeatability parameters and position accuracy parameters shown in Table VII can be obtained.

Taking the maximum value of the position repeatability of each point, it can be seen that the position repeatability of the redundantly actuated parallel robot is 0.053 mm, and the position accuracy is 0.635 mm.

The end load of the robot is set to 10 kg, 20 kg, 30 kg, 40 kg, 50 kg, and 60 kg, respectively, for precision measurement, and the position repeatability parameters and position accuracy parameters shown in Table VIII can be obtained.

## 6. Conclusion

In order to meet the demands of high-precision and high load-bearing capacity applications, this paper addresses the issues of limited good workspace, high singularity occurrence, and restricted load-bearing capacity in non-redundant parallel mechanisms. To tackle these challenges, a fully redundant drive parallel mechanism was designed and developed. The study encompassed the investigation of performance evaluation metrics, identification of good workspace, and scale optimization design. The following conclusions were drawn:

(1) Performance evaluation metrics for motion/force transmission were established. Through comparisons, it was determined that under the fully redundant drive mode, the GTW area of the planar 6R mechanism increased by 5.45, representing a growth magnitude of 136 times, with  $LTI \geq 0.7$ .

(2) Scale optimization was carried out for the planar 6R parallel mechanism. The optimized mechanisms exhibited larger GTW areas, and GTI values were consistently above 0.87.

(3) The control strategy of the mechanism has been studied. Experimental results demonstrated a maximum load capacity of 120 kg, with a payload-to-weight ratio of 15.83%. Position repeatability and positional accuracy were measured at 0.053 mm and 0.635 mm, respectively, for a 120-kg load. For a 60-kg load, position repeatability and positional accuracy were 0.079 mm and 0.733 mm, respectively. These results substantiate that the designed redundant drive parallel mechanism can meet the demands for high-load and high-precision assembly.

The outcomes of this research contribute to enhancing the performance evaluation and scale optimization framework for redundant drive parallel mechanisms. Furthermore, they hold significant practical implications for the widespread application of redundant drive parallel mechanisms in heavy-duty assembly and other construction-related fields.

**Author contributions.** Dong Yang and Ming Han conceived and designed the study and translated the article. Jiajin Che performed statistical analyses and wrote the article. Jinyue Liu assisted Jiajin Che in completing prototype experiments.

**Financial support.** This work was supported by the Central Leading Local Science and Technology Development Fund Project (Grant No. 236Z1910G) and the Postdoctoral Research Project in Hebei Province (Grant No. B2023005005).

**Competing interests.** The author(s) declare(s) that there is no competing interests regarding the publication of this paper.

**Ethical approval.** None.

## References

- [1] L. Wang, Z. Zhang and Z. Shao, “Kinematic performance analysis and promotion of a spatial 3-RPaS parallel manipulator with multiple actuation modes,” *J Mech Sci Technol* **33**(2), 889–902 (2019).
- [2] S. Lee, S. Kim, W. In, M. Kim, J. I. Jeong and J. Kim, “Experimental verification of antagonistic stiffness planning for a planar parallel mechanism with 2-DOF force redundancy,” *Robotica* **29**(4), 547–554 (2011).
- [3] L. Xu, Q. Li, N. Zhang and Q. Chen, “Mobility, kinematic analysis, and dimensional optimization of new three-degrees-of-freedom parallel manipulator with actuation redundancy,” *J Mech Robot* **9**(4), 041008 (2017).
- [4] J. H. Choi, T. W. Seo and J. W. Lee, “Torque distribution optimization of redundantly actuated planar parallel mechanisms based on a null-space solution,” *Robotica* **32**(7), 1125–1134 (2014).
- [5] D. X. Zeng, Y. L. Hou and Z. Huang, “Type synthesis and characteristic analysis of a family of 2-dof rotational decoupled parallel mechanisms,” *Chin J Mech Eng* **22**(6), 833–840 (2009).
- [6] B.-J. Yi, S.-R. Oh and I. H. Suh, “A five-bar finger mechanism involving redundant actuators: Analysis and its applications,” *IEEE Trans Robot Automat* **15**(6), 1001–1010 (1999).
- [7] L. Wang, Z. Zhang and Z. Shao, “Kinematic performance analysis and promotion of a spatial 3-RPaS parallel manipulator with multiple actuation modes,” *J Mech Sci Technol* **33**(2), 889–902 (2019).
- [8] S. H. Li, J. Sun and Y. X. Shan, “Optimization of novel parallel pointing mechanism for space optical mirror,” *Guangxue Jingmi Gongcheng/Optics and Precision Engineering* **27**(3), 637–644 (2019).
- [9] Z. Gao and D. Zhang, “Workspace representation and optimization of a novel parallel mechanism with three-degrees-of-freedom,” *Sustainability* **3**(11), 2217–2228 (2011).
- [10] Y. Zhou, F. Xie and X. Liu, “Optimal design of a main driving mechanism for servo punch press based on performance atlases,” *Chin J Mech Eng* **26**(5), 909–917 (2013).
- [11] X. S. Yang, Z. L. Zhao and H. Xiong, “Kinematic analysis and optimal design of a novel schfnlies-motion parallel manipulator with rotational pitch motion for assembly operations,” *J Mech Robot* **13**(4), 1–17 (2021).
- [12] S. N. Nabavi, M. Shariatee, J. Enferadi and A. Akbarzadeh, “Parametric design and multi-objective optimization of a general 6-PUS parallel manipulator,” *Mech Mach Theory* **152**, 103913 (2020).
- [13] A. Antonov, A. Fomin, V. Glazunov and Ceccarelli M., “Workspace and performance analysis of a 6-DOF hexapod-type manipulator with a circular guide,” *Proceed Inst Mech Eng, Part C: J Mech Eng Sci* **236**(18), 9951–9965 (2022).
- [14] C. Yang, W. Ye and Q. Li, “Review of the performance optimization of parallel manipulators,” *Mech Mach Theory* **170**, 104725 (2022).
- [15] H. T. Liu, T. Huang and A. Kecskeméthy, Force/motion/stiffness transmissibility analyses of redundantly actuated and overconstrained parallel manipulators, *nephron clinical practice*, (2015) 609–618.
- [16] L. Wang, Z. Zhang, Z. Shao and X. Tang, “Analysis and optimization of a novel planar 5R parallel mechanism with variable actuation modes,” *Robot Com-Int Manuf* **56**, 178–190 (2019).
- [17] H.-Q. Zhang, H.-R. Fang and B.-S. Jiang, “Motion-force transmissibility characteristic analysis of a redundantly actuated and overconstrained parallel machine,” *Int J Auto Comp* **16**(2), 150–162 (2019).
- [18] M. Mazare and M. Taghizadeh, “Geometric optimization of a delta type parallel robot using harmony search algorithm,” *Robotica* **37**(9), 1494–1512 (2019).
- [19] R. Desai and S. Muthuswamy, “A forward, inverse kinematics and workspace analysis of 3RPS and 3RPS-R parallel manipulators,” *Iranian J Sci Tech, Trans Mech Eng* **45**(1), 115–131 (2021).
- [20] H. Yang, H. Fang, Y. Fang and X. Li, “Dimensional synthesis of a novel 5-DOF reconfigurable hybrid perfusion manipulator for large-scale spherical honeycomb perfusion,” *Front Mech Eng* **16**(1), 46–60 (2021).
- [21] Y. Yang, Y. Tang, H. Chen, Y. Peng and H. Pu, “Mechanism design and parameter optimization of a new asymmetric translational parallel manipulator,” *Mech Sci* **10**(1), 255–272 (2019).

- [22] L. J. Zhang, F. Guo and Y. Q. Li, "Optimum design of parallel mechanism based on kinematics distribution performance," *Nongye Jixie Xuebao/Trans Chinese Soci Agri Mach* **46**(4), 365–371 337 (2015).
- [23] X.-J. Liu and J. Wang, "A new methodology for optimal kinematic design of parallell mechanisms," *Mech Mach Theory* **42**(9), 1210–1224 2007 (2007).
- [24] B. Zhu, L. Wang and J. Wu, "Optimal design of loading device based on a redundantly actuated parallel manipulator," *Mech Mach Theory* **178**, 105084 (2022).
- [25] V. A. Glazunov, V. Arkaelyan, S. Briot and G. V. Rashoyan, "Speed and force criteria for the proximity to singularities of parallel structure manipulators," *J Mach Manuf Reliab* **41**(3), 194–199 (2012).
- [26] S.-H. Wen, W. Zheng, S.-D. Jia, Z.-X. Ji, P.-C. Hao and H.-K. Lam, "Unactuated force control of 5-DOF parallel robot based on fuzzy PI," *Int J Control Autom Syst* **18**(6), 1629–1641 (2020).
- [27] T. Haitao, L. Shunpan and Y. Jiantao, "Hybrid force/Position control hardware systemDesign and force servo control realization," *Adv Mat Res* **317**, 685–689 (2011).